ORIGINAL ARTICLE

Seismotectonics of SE Aegean inferred from precise relative locations of shallow crustal earthquakes

R. Andinisari ⬤ **· K. I. Konstantinou · P. Ranjan**

Abstract We relocated the seismicity in SE Aegean that was recorded by both permanent and temporary seismic networks during 2004–2018 in order to investigate its correlation with the active faults in this area. P and S-phase travel times of best quality events were used to estimate a minimum 1D velocity model with station delays by utilizing VELEST. This velocity model and station delays were then used to obtain absolute locations of 3055 events, utilizing the probabilistic nonlinear algorithm NLLOC. The double-difference algorithm was used along with catalog and cross-correlation differential times to relocate all the events, resulting in 2200 precise relative locations with horizontal and vertical uncertainties of less than 1.0 km. The precise

locations delineated faults along the Gulf of Gökova, SW of Nisyros, and Karpathos area. Based on the comparison of the resulting seismicity distribution with the regional stress field, it can be concluded that seismicity only occurred along faults with ENE-WSW strike in the area north of Tilos and N-S strike in the area south of Tilos. Seismogenic layer thickness estimated from the hypocentral depth distribution was found to vary between 12.1 and 15.4 km. Expected moment magnitudes of faults in this area were calculated by using their geometrical properties and the seismogenic layer thickness, yielding magnitudes in the range of 5.9–6.9. The fact that most of the seismically active faults in SE Aegean lie offshore increases the probability that a major earthquake will be followed by a tsunami and calls for the close monitoring of seismicity in this area.

Article Highlights
• As many as 2200 crustal earthquakes in South East Aegean have been precisely relocated.
• The estimated seismogenic layer thickness in the area is 12.1–15.4 km.
• Expected magnitudes of future earthquakes in South East Aegean vary between 5.9 and 6.9.

R. Andinisari (✉) · K. I. Konstantinou · P. Ranjan
Department of Earth Sciences, National Central University,
Chungli, Taoyuan, Taiwan
e-mail: ratriandini@g.ncu.edu.tw

P. Ranjan
Taiwan International Graduate Program–Earth System Science
(TIGP–ESS), Taipei, Taiwan

1 Introduction

The Aegean region exhibits significant tectonic activity as a result of several geodynamic processes. One of these processes is the subduction of the African lithospheric plate beneath the Aegean at the rate of about 0.9 cm/year (Reilinger et al. 2006; McClusky et al. 2000), forming the Hellenic subduction zone (Fig. 1). The African plate is subducting beneath the Aegean with an increasing degree of obliquity from the western to the eastern part with a maximum value of 40° to 50°

(Bohnhoff et al. 2005). The Aegean microplate is dragged in a southwestward direction at a rate of 3.5 cm/year due to the slab rollback of the African plate (Hollenstein et al. 2008; Nyst and Thatcher 2004; Reilinger et al. 2006; Rontogianni 2010). The SE Aegean in particular experiences significant extensional deformation (Rontogianni 2010) characterized by ENE-WSW trending normal faulting along the Gulf of Gökova (Kurt et al. 1999) as well as N-S normal faulting to the north of Karpathos island. However, there is no significant extensional deformation observed in the area around Rhodes island (Hall et al. 2009). The dominance of extensional regime in SE Aegean is also supported by GPS observations showing an increase in the velocity field towards the Pliny-Strabo trenches, relative to central Aegean and Peloponnese (Reilinger et al. 2010). Aside from that, the SE Aegean also hosts the active Nisyros caldera that produced several eruptions in the past and during 1995-1997 it also experienced a period of unrest.

From the point of view of historical seismicity, the SE Aegean region has a rich record of large earthquakes. Based on the ISC-GEM catalog (Storchak et al. 2013) and the catalog of the National Observatory of Athens (NOA), as many as 15 earthquakes with moment magnitude varying between 5.5 and 7.3 have been recorded from the year 1911 up until 2017 (Table 1). Among these earthquakes, there were 3 events with moment magnitude of 6.4 or larger (Fig. 1). The first of these events is the Kos earthquake that occurred on 23 April 1933 with a moment magnitude of 6.4. This earthquake was felt in the islands of Kos and Nisyros, as well as in broad areas along the Turkish coast. Other than causing a tsunami that affected Kos island, this earthquake also caused the death of 200 people with 600 others injured (Papazachos and Papazachou 2003). The second large earthquake occurred on 9 February 1948 to the east of Karpathos with moment magnitude of 7.3 (Ebelling et al. 2012). This earthquake destroyed 573 houses and excited a tsunami that inundated the coast up to 1 km (Papazachos and Papazachou 2003). The latest destructive earthquake in the SE Aegean occurred on 20 July 2017 with magnitude of 6.6 and was located in Gökova graben between the city of Bodrum and the island of Kos. Hence, this event will be referred to as the Bodrum-Kos earthquake hereafter. The rupture zone of this earthquake could not be observed directly since it was located offshore. Besides from generating a small tsunami and causing heavy damages in Bodrum

peninsula and on Kara Ada island, the Bodrum-Kos earthquake also caused the death of 2 people in Kos island. Based on these observations, it can be easily understood that SE Aegean is an area significantly exposed to both seismic and tsunami hazards.

The main purpose of this work is to relocate the shallow crustal seismicity in SE Aegean in order to investigate the geometry and segmentation characteristics of active faults in this area. The resulting information will later be used to determine the seismogenic layer thickness and assess the potential seismic hazard. First, a minimum 1D velocity model was estimated from the well-recorded earthquakes and was then utilized to obtain absolute earthquake locations. The resulting absolute locations were then compared to routine locations provided by NOA to assess their differences. Subsequently, precise relative relocation was performed and the resulting seismicity distribution was analyzed in the interest of delineating active faults in the area, and for the purpose of examining the correlation of the resulting seismicity distribution with the prevailing regional stress field. Finally, we combined historical seismicity information with the delineated faults to study several seismogenic sources in the area in terms of their potential to generate strong earthquakes in the future.

2 Data

The data that we used was recorded by permanent and temporary networks deployed in the southern Aegean and SW Turkey. These networks are Hellenic Seismic Network (HL) (National Observatory of Athens, Institute of Geodynamics, Athens 1997), the Hellenic Unified Seismic Network (HUSN), KOERI seismic network (Boğaziçi University Kandilli Observatory and Earthquake Research Institute 2001), and the EGELADOS (Exploring the Geodynamics of Subducted Lithosphere Using an Amphibian Deployment of Seismographs) network (Friederich and Meier 2005). HL consisted of only 26 seismic stations which were equipped with 20–120 s three-component broadband seismometers. This seismic network was merged with other permanent seismic networks in Greece to form HUSN in 2008. From August 2004 to January 2005, a series of events originated in the Gulf of Gökova were recorded by HL and stations that belonged to KOERI. As many as 41 crustal events from the mentioned period with moment magnitude between 4.0 and
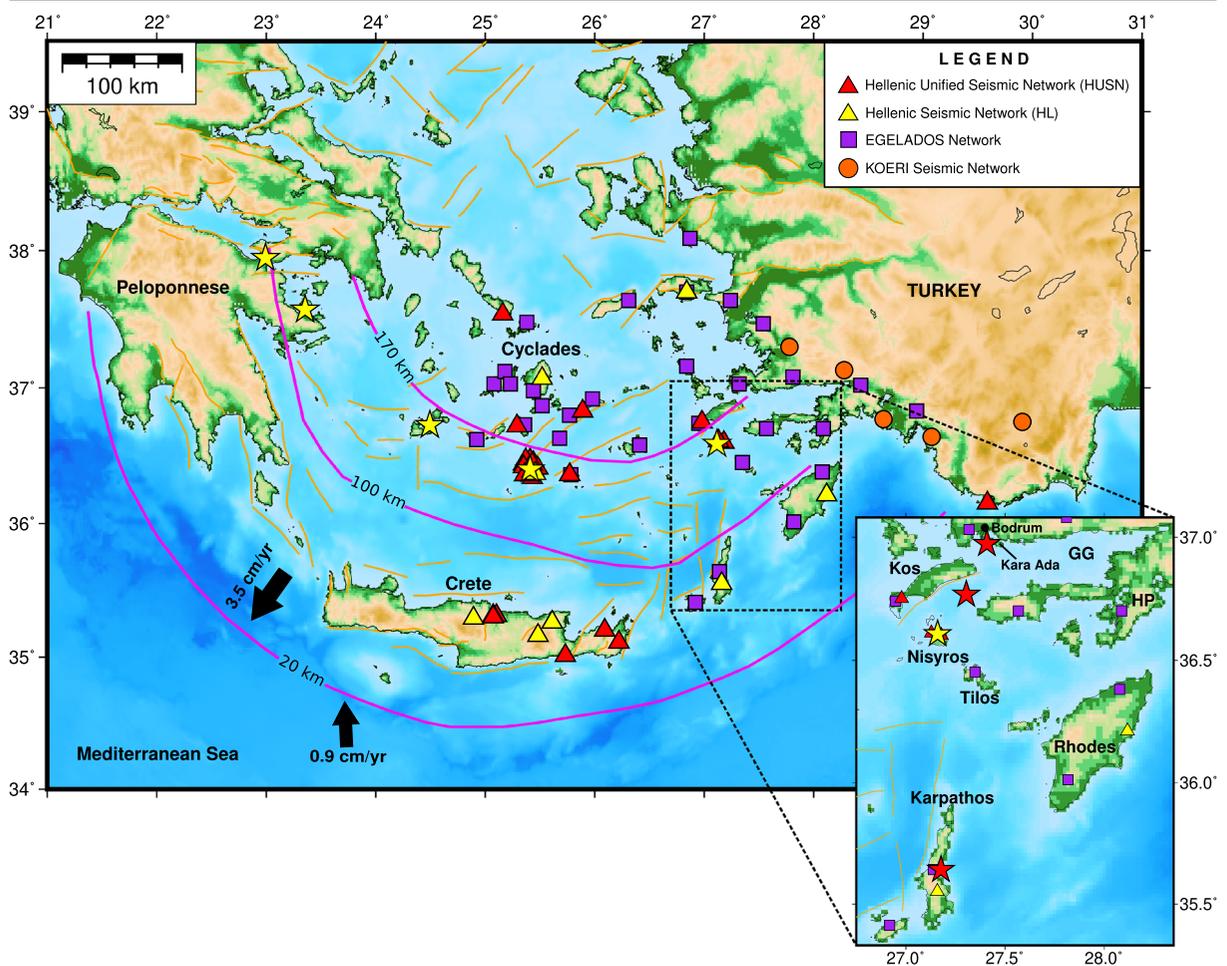
Fig. 1 Map of south Aegean with the study area highlighted in the dashed square. Solid orange lines represent active faults contained in the GReDaSS database (Caputo and Pavlides 2013). The magenta lines show isodepth curves of earthquake hypocenters that occurred along the Wadati-Benioff zone (Papazachos et al. 2000). The thick black arrows represent the present-day plate motions. The yellow stars indicate the locations of active volcanic centers.

Inset map in the bottom right corner shows a detailed map of the study area. GG and HP in inset map represent the Gulf of Gökova and Hisarönü Peninsula, respectively. Red stars in inset map indicate the location of 3 earthquakes with moment magnitude 6.4 or larger that occurred in SE Aegean within the period of 1911–2017

5.5 were used in this study. We also included 30 other events recorded by KOERI and HL/HUSN for the period of March 2006 to November 2010. These events also occurred in the Gulf of Gökova with magnitudes ranging from 3.3 to 4.8. The inclusion of these events in our analysis was based on the fact that they occurred in the central and eastern part of the gulf where fewer events were recorded in the following years. We obtained the waveforms of all these events and manually picked their phases. In October 2005 to March 2007, the EGELADOS network was deployed in the southern Aegean. This network extended from Peloponnese to SW Turkey and consisted of 56 stations equipped with broadband three-components sensors (45 Güralp 60-s

seismometers, 4 STS-2 seismometers, and also 7 1-Hz Mark seismometers). The EGELADOS network also included permanent stations of the GeoForschungsNetz (GEOFON) network equipped with short period three-component seismometers and 1 Mediterranean Very Broadband Seismographic Network (MedNet) station. As many as 740 crustal events that occurred in our study area were recorded by this network during its functional period and their phases were also manually picked. The strongest earthquakes that were recorded by EGELADOS network in our study area have magnitudes of 4.0–4.4. A large portion of our data consists of crustal earthquakes recorded by HUSN. Established in 2008, this seismic network consists of 153 stations

Table 1 Source parameters of earthquakes with moment magnitude of 5.5 or larger that occurred in SE Aegean from the year 1911 until 2017. OT is the origin time of each earthquake in UTC. The letter "f" next to the value of the hypocentral depth indicates that the hypocenter was fixed. ΔM is the uncertainty of the moment magnitude for each earthquake

Date	OT	Lat	Lon	H (km)	Mw	ΔM	Reference
1911-04-30	20:42:27.89	36.80	27.68	15f	5.6	0.20	ISC-GEM
1918-07-16	20:03:39.05	36.59	27.04	15f	5.9	0.42	ISC-GEM
1921-01-27	11:30:24.85	36.85	27.99	15f	5.5	0.20	ISC-GEM
1933-04-23	05:57:34.97	36.76	27.30	15f	6.4	0.32	ISC-GEM
1941-12-13	06:16:02.95	36.81	27.95	15f	6.0	0.20	ISC-GEM
1942-02-02	17:05:30.17	36.29	28.10	15f	5.7	0.22	ISC-GEM
1942-06-21	04:38:33.74	36.03	26.97	15f	5.5	0.20	ISC-GEM
1943-10-16	13:08:46.77	35.99	27.73	15f	5.7	0.43	ISC-GEM
1944-01-05	07:44:06.59	36.27	27.80	15f	5.7	0.20	ISC-GEM
1948-02-09	12:58:18.43	35.64	27.16	15f	7.3	0.20	ISC-GEM
1948-02-12	22:27:15.13	35.85	27.43	15f	5.6	0.22	ISC-GEM
1948-10-18	08:59:57.41	35.61	27.30	15f	5.7	0.20	ISC-GEM
1952-10-22	04:14:56.00	36.39	27.77	15f	5.5	0.20	ISC-GEM
1968-12-05	07:52:11.58	36.48	26.99	20	6.1	0.30	ISC-GEM
2017-07-20	22:31:11.71	36.96	27.43	6	6.6	-	NOA

equipped with 30–120-s three-component broadband seismometers with various types of sensors, such as CMG-3ESPC, CMG-3T, CMG-40T, STS-1, STS-2, Le-3D, KS2000M, and TRILLIUM 120p. All events recorded by HUSN are relayed to NOA in order to be processed further. The basic processing includes phase picking and earthquake location, as well as moment tensor determination using waveform inversion. The P and S-phase arrivals of these events are picked by NOA staff and a weight factor is also assigned to every phase pick. Most of the P-phase picks are assigned 0-1 weight factor indicating best quality picks, whereas most of the S-phase picks are assigned 2-3 weight factor. As many as 2244 crustal earthquakes were recorded by this seismic network from January 2011 to June 2018. Except from the Bodrum-Kos earthquake, all other events have local magnitudes between 1.2 and 5.1 as determined by NOA. In order to ensure the accuracy of the picks, manual phase repicking has been done whenever necessary.

3 Estimation of minimum 1D model

In order to obtain precise locations for all of our events, we derived a minimum 1D velocity model for our study area. The minimum 1D velocity model was estimated by inverting P and S-wave travel times together with the hypocentral locations and station delays by using VELEST (Kissling et al. 1994). The algorithm VELEST estimates the most appropriate solution for the coupled hypocenter-velocity problem for any given set of earthquakes, resulting in a minimum 1D velocity model with station delays. The events that are used to derive a minimum 1D model must provide good coverage of the study area and must conform to these criteria: (a) the number of observed phase picks should be more than 8 with at least 4 S-phase picks, (b) the RMS residual should be less than 0.5 s, and (c) the azimuthal gap should be less than 180°. Seismic stations used for the inversion are the ones located 200 km or less from the center of our study area, consisting of 25 stations of HUSN and 16 stations of EGELADOS Network. This selection yielded 298 events recorded by EGELADOS network and 92 events recorded by HUSN with a total number of 4561 P-phase and 2586 S-phase readings. The number of P and S-phases of each station can be found in Table S1 in Online Resource. The reference station chosen is TILO (36.4485° N and 25.3535° E) which is installed on limestone. In the later analysis, the knowledge of near-surface geology of the reference station can be used to qualitatively interpret geological structure beneath the other stations. The P-wave delay of the reference station will be fixed to zero during the

inversion. Hence, the resulting station delays indicate whether the geological structure beneath a particular station consists of harder or softer rocks relative to the structure of the reference station. The layers used for the initial model were set to be 2 km thick from the surface down to the depth of 30 km and layer thickness of 5 km was used for the depth below 30 km.

In a coupled hypocenter-velocity problem, several local RMS misfit minima may occur. To make sure that we have obtained a velocity model that is associated with a robust minimum, probing a larger solution space is required. In order to do this, we performed multiple VELEST runs with various models as suggested by Kissling et al. (1994). We used a P-velocity model proposed by Papazachos et al. (2000) as the initial model. Then, we created as many as 80 new initial models for P-velocity by shifting the initial model by as much as ± 5%, ± 10%, and ± 15% of its original values. Random numbers between − 1.0 and 1.0 were then added to the velocity of each layer of these shifted initial models. Figure 2 shows all the initial P-velocity models as well as the resulting models together with their RMS misfits. The final P-velocity model was obtained by averaging 5 resulting models with the lowest RMS misfits (0.299–0.306 s). Another VELEST run was then performed to invert for S-velocity by fixing the final P-velocity model. In the S-velocity estimation, the occurrence of any low-velocity layers was not allowed as this would introduce more nonlinearity to the inversion problem.

Based on the estimated P and S-velocity model, the Vp/Vs value as a function of depth can also be calculated (Fig. 3). While the P and S-velocities are increasing slowly from the depth of 4 down to 18 km, the Vp/Vs ratio stabilizes around the value of 1.73 in this depth range only to greatly fluctuate at 20–30 km. Our new P-velocity model agrees quite well with the P-velocity model of Brüstle (2012), with noticeable differences at depths of 20 km and ~ 30 km. Our P-velocity model is faster by 6.8% and 18% at depths of ~ 20 km and ~ 30 km, respectively. Other than that, the differences between both P-velocity models in the other layers are in the order of 0.1–5.2%. We also compared the newly estimated S-velocity model to the S-velocity model derived from Rayleigh wave dispersion by Karagianni et al. (2005). The major difference between the two models can be found at depths 10–16 km where the model of Karagianni et al. (2005) indicates the existence of a low-velocity layer. Besides this, there are also more

than 20% differences in velocity values at depths less than 4 km and deeper than 30 km. At the shallow depths, the layers are subvertically penetrated by the seismic rays. On the other hand, smaller number of seismic rays penetrated the layers at depths greater than 30 km (Fig. 3). Thus, our newly estimated minimum 1D model is not well constrained at depths of less than 4 km and also deeper than 30 km.

It should be noted that the inclusion of all the seismic stations (at distances more than 200 km) in the velocity inversion will result in a similar 1D velocity model since the majority of the selected events are of small magnitude and are less likely to be recorded by seismic stations located more than 200 km away. The comparison of minimum 1D velocity model estimated by using all the available stations in southern Aegean and stations located 200 km or less from the center of our study area is shown in Fig. S1 in Online Resource. The similarity of these models, however, does not extend deeper than 22-km depth. The absence of deep propagating seismic rays which were recorded by stations located more than 200 km away may be causing the differences in the resulting P and S-velocities for layers deeper than 22 km.

One way to assess the robustness of the resulting minimum 1D model is by using a perturbation test for the initial hypocentral locations. This test is performed by shifting the initial locations randomly by 5 km and then using this as an input for a single VELEST run together with the obtained minimum 1D model. If both station delays and the minimum 1D model denote a robust minimum, the resulting locations will be having small difference compared to the initial ones. From this test, we find that the average location shift for longitude, latitude, and depth are 0.13 km (± 0.40 km), − 0.02 km (± 0.30 km), and 1.47 km (± 1.31 km), respectively (Fig. S2 in Online Resource). Another way to assess the robustness of a minimum 1D velocity model is by matching the resulting values of station delay with the geological structure beneath every station. Stations with negative station delay values should lie on local high-velocity rocks with respect to the reference station. On the contrary, stations with positive station delay values should lie on low-velocity materials (softer rocks). In order to make the assessment process easier, the stations are divided into three categories based on the near-surface geology. These three categories are hard rocks, soft rocks, and alluvium. The hard rocks category includes granite, lavas, limestone, marble, and gneiss,

Fig. 2 The 80 initial P-wave velocity models versus depth and the final P-wave velocity models derived using VELEST. The gray lines represent randomized initial P-velocity models. Colored lines represent final P-velocity models as a function of RMS misfit based on the color scale at the right. The blue line represents the stable P-velocity model calculated by averaging 5 final P-velocity models with lowest RMS misfit
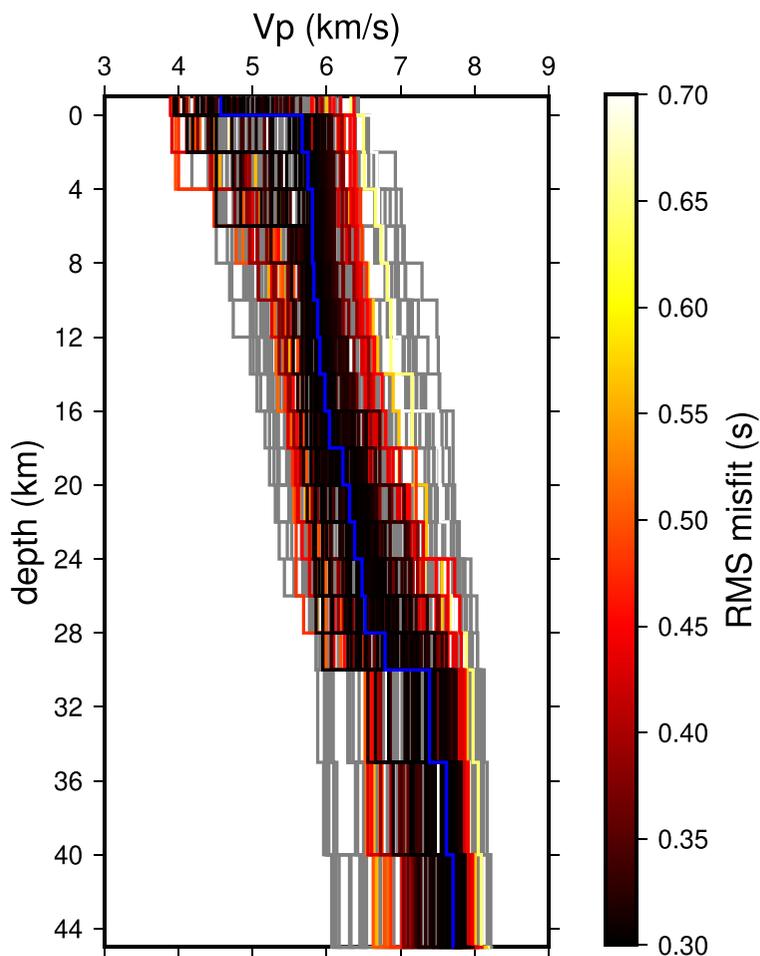
whereas soft rocks category consists of sedimentary deposits and tuffs. The stations located in the Cyclades have mostly negative station delays for both P and S-wave arrivals, while the ones located in SE Aegean and eastern Crete have zero to positive station delays. This result is consistent with the geological setting of Cyclades which predominantly consists of metamorphic rocks, while most of the stations in SE Aegean are situated on top of alluvium deposits and soft rocks (tuffs). A map of the station delays with matched near-surface geological structure for each station is shown in Fig. S3 in Online Resource.

4 Absolute locations

In this study, we used the NLLOC package (Lomax et al. 2000) along with the new minimum 1D velocity model and its station delays to obtain absolute locations for all the events in SE Aegean. NLLOC estimates absolute earthquake locations by utilizing the probabilistic formulation proposed by Tarantola and Valette (1982). Based on this formulation, the most probable location of an earthquake can be estimated from a set of points of the posterior Probability Density Function (PDF). The optimal hypocenter location is then approached by finding the maximum likelihood point of the PDF through the Oct-tree search algorithm (Lomax and Curtis 2001). In this study, we also utilized the Equal Differential-Time (EDT) likelihood function (Font et al. 2004) which is generated from the differences of residuals of an event recorded at a pair of stations. The usage of PDF complemented with EDT likelihood function will result in a robust location even in the presence of large outliers in the observed travel times.

Prior to locating all the earthquakes, a 3D grid must be constructed that is encompassing the study area as
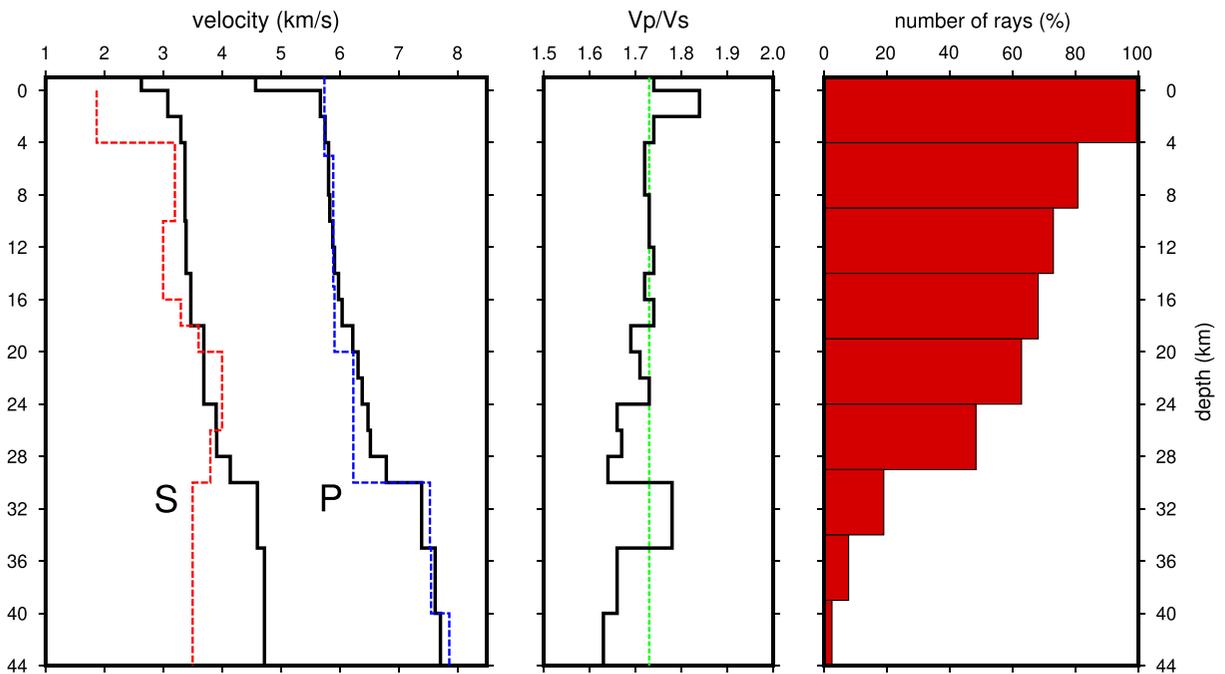
Fig. 3 Final 1D velocity model along with the corresponding Vp/Vs ratio and percentage of rays passing through every layer. The solid black lines in the left panel are the P and S-velocity, while the dashed red and blue lines are the S-velocity model of Karagianni et al. (2005) and the P-velocity model of Brüstle (2012), respectively. The green line in the middle panel indicates the Vp/Vs ratio of 1.73 which is expected for a Poisson solid

well as all of the stations. The chosen 3D grid for this study is 1900 × 900 × 80 cells with 1 × 1 × 1-km node spacing. This 3D grid was then used to calculate theoretical travel times for every station. This calculation was carried out by using the finite differences algorithm of Podvin and Lecomte (1991). The covariance matrix was utilized to calculate the horizontal (ERH) and vertical uncertainties (ERV) for the resulting absolute locations (Maleki et al. 2013). Both ERH and ERV values depend on the shape of the PDF and will become large if the PDF deviates from ellipsoidal shape. Figure 4 shows the absolute locations obtained using NLLOC as a function of depth, ERH, and ERV.

Prominent seismicity can be seen along the Gulf of Gökova, with earthquakes concentrated in the western part of the gulf. This concentrated cluster of earthquakes was mainly caused by the mainshock of the Bodrum-Kos earthquake and its aftershocks. Several events were also located in the eastern part of the gulf which correspond to the earthquakes that occurred from August 2004 to January 2005. Smaller clusters of earthquakes can also be found in the Hisarönü Peninsula and SW of Nisyros. In the southern part of our study area, earthquakes can be found in the east and west of Karpathos island with most events

concentrated to the north of the island. On the other hand, the islands of Tilos and Rhodes are almost free of seismicity.

The overall absolute earthquake locations in the study area yielded average RMS residual of 0.35 s (± 0.63 s). The average ERH and ERV values are 5.06 km (± 4.20 km) and 5.67 km (± 5.04 km), respectively. Based on the distribution of ERH and ERV values (Fig. 4), the events with smaller uncertainties are the ones that were located in the Gulf of Gökova, around Nisyros area, to the west of Rhodes, and to the north of Karpathos. The uncertainties of the events located in the southern part of the study area are generally larger. This might be caused by the smaller number of seismic stations located in the southern part of the area compared to the northern part.

Since NOA also provides routine locations for earthquakes in the Aegean, a comparison between probabilistic nonlinear locations and NOA routine locations can be performed. The locations used for this comparison are the absolute locations of events recorded by HUSN excluding the absolute locations of events recorded by HL, KOERI, and EGELADOS network. The quantities we chose for this comparison were RMS residuals and the hypocentral depths. RMS residual indicates the quality of
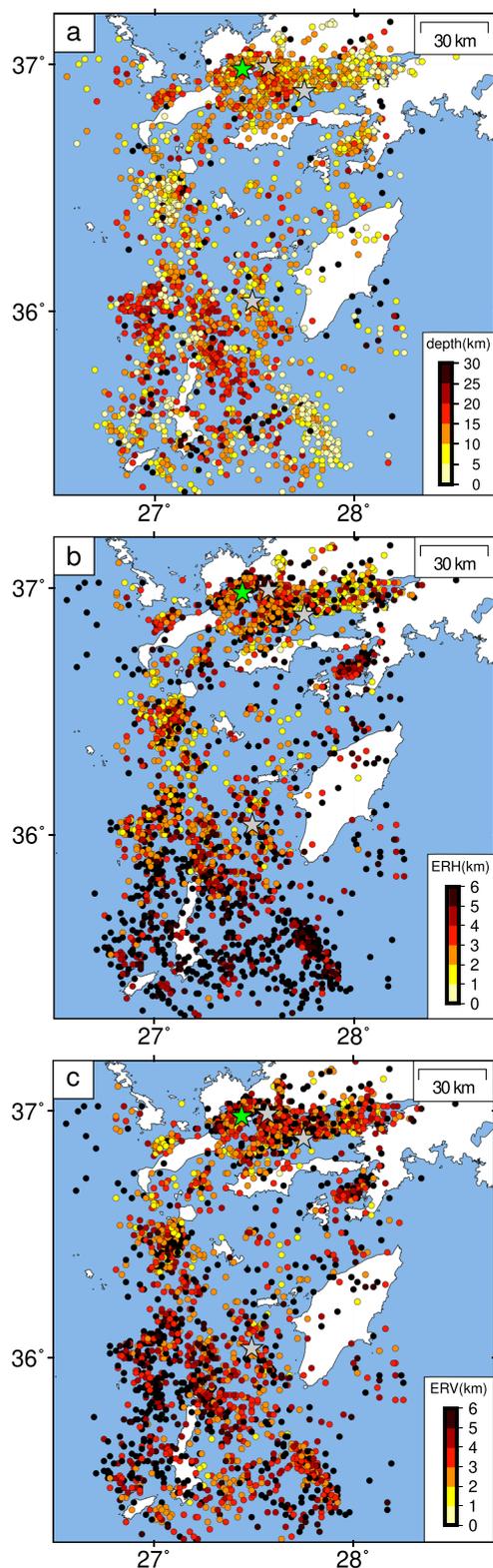
Fig. 4 Results of absolute relocation for all the events in the study area. Green star represents the location of the recent large earthquake on 20 July 2017 and the gray stars represent earthquakes with moment magnitude 5.0 or larger. The absolute locations are plotted as a function of (**a**) hypocentral depth, (**b**) horizontal uncertainty or ERH, and (**c**) vertical uncertainty or ERV

the resulting absolute locations and the suitability of the velocity model used for the location. On the other hand, the hypocentral depth is the most difficult parameter to constrain in the earthquake location problem. Figure 5 shows the comparison between the RMS residuals and hypocentral depths of NOA routine locations and NLLOC locations. The RMS residuals of NOA locations range from 0.01 to 0.98 s with average value of 0.37 s (± 0.13 s), while the RMS residuals of events recorded by HUSN and relocated by using NLLOC is 0.39 s (± 0.71 s). Even though the average RMS residuals of the NOA routine locations show smaller values compared to the NLLOC locations, the hypocentral depths are significantly different. The average hypocentral difference between NOA and NLLOC locations is 11.64 km (± 8.31 km), while the average epicentral difference is much smaller (0.72 ± 1.53 km). The hypocentral depths of absolute locations obtained by NLLOC lie mostly above 16 km. This result agrees well with the Moho in this area which lies between 20 and 26 km (Karagianni et al. 2005; Sodoudi et al. 2006; van der Meijde et al. 2003; Tirel et al. 2004). On the contrary, the hypocentral depths of NOA routine locations are concentrated around 10–16 km and 24–30 km with several events deeper than 30 km. This bimodal distribution of NOA hypocentral depths has been also observed along the North Aegean Trough (Konstantinou 2017) and in NE Aegean (Konstantinou 2018). According to synthetic tests done by Konstantinou (2017), NOA uses a relatively simple velocity model which only consists of two layers over a half-space and this may be causing shallow events to be located 7–10 km deeper than their true locations. While this partly explains the occurrence of events slightly below the Moho in NOA locations, it cannot explain the occurrence of events deeper than 26 km.

5 Relative locations

5.1 Method

The double-difference algorithm, or HYPODD, of Waldhauser and Ellsworth (2000) can be used to enhance the obtained locations from the previous section.
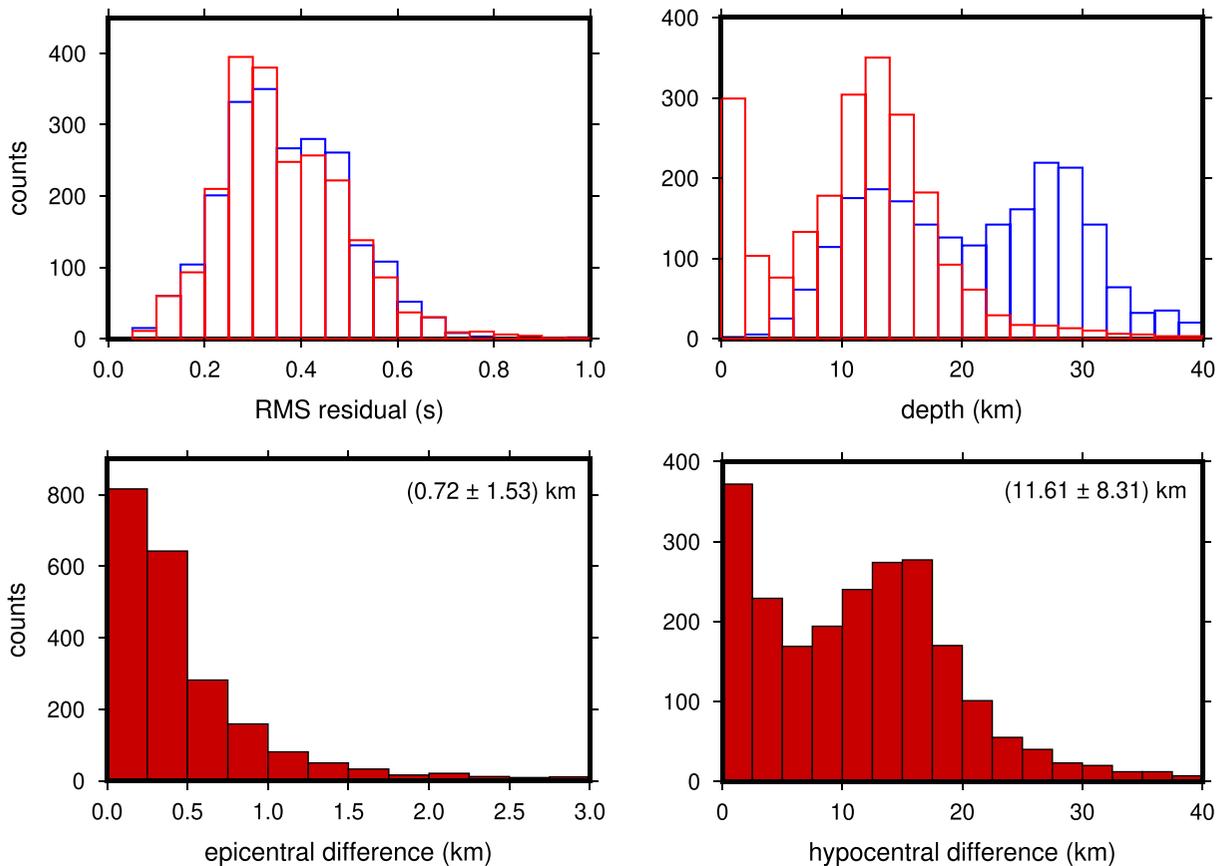
Fig. 5 Histograms showing the comparison of RMS residual and depth distribution of NOA and NLLOC locations (top panel) and epicentral as well as hypocentral differences between NOA and NLLOC locations (bottom panel). The blue and red bars in the top panels represent NOA locations and NLLOC locations, respectively. The numbers in the upper right corner of each histogram in the bottom panel show the average value and standard deviation of each distribution

The basic concept of this algorithm is to adjust the discrepancy of hypocentral distance between two earthquakes as long as its value is smaller compared to the distance of both earthquakes to a common station. This algorithm makes use of catalog travel time differences or both catalog and waveform cross-correlation differential times. Catalog travel time differences can be obtained by constructing a network of links between events so that a chain of well-connected events from one event to any other event could be obtained (Waldhauser 2001). The search radius was set to 15 km for stations 200 km away from earthquake sources and each event was required to have 8 neighboring events so that the resulting link is well connected. These parameters yielded a total of 3055 events, with the network of links consisting of 704,385 P-phase and 350,484 S-phase pairs. The calculation of differential travel times resulted in an average number of 8 links per

event pair and average offset between linked events of 8.97 km. There were approximately 17% weakly linked events and 2% outliers which indicates that the data have relatively good quality. To increase the precision of the relocation, catalog travel time differences were used along with the cross-correlation differential times of any event pairs with cross-correlation coefficient higher than 0.7 (Fig. S4a in Online Resource). For the waveform cross-correlation, we used a window length of 2 s for the P-wave and 3 s for the S-wave, while we first lowpass filtered the waveforms using a corner frequency of 5 Hz. The waveform cross-correlation was performed by using a modified version of the multi-channel cross-correlation method of VanDecar and Crosson (1990). The velocity model used in the relative relocation is the P-velocity model from the previous section along with Vp/Vs ratio of 1.72. This Vp/Vs ratio was obtained by averaging all the Vp/Vs

values obtained from the minimum 1D model down to a depth of 40 km (Fig. 3). We also utilized a Wadati diagram in order to calculate the Vp/Vs ratio which yielded again a value of 1.72 (Fig. S5 in Online Resource).

Since we had to relocate a large number of earthquakes, the LSQR conjugate gradients method was chosen as it is computationally more efficient. The damping parameter was set to 80 as this value produced condition numbers between 40 and 80 for the majority of obtained event clusters as suggested by Waldhauser (2001). The catalog data were given higher a priori phase weightings in order to obtain the relative position of all the events during the first five iterations; then, they were down-weighted relative to the cross-correlation data during the next five iterations to improve the location of event pairs with small separation distances (Waldhauser 2001). A total of 2200 events were successfully relocated (~ 72%) with an average RMS residual of 0.26 s (± 0.32 s). This value is lower compared to the average RMS residual for the absolute locations obtained with NLLOC, which is 0.35 s. LSQR does not produce accurate error estimates, therefore location uncertainties are estimated by relocating smaller earthquake clusters using the Singular Value Decomposition (SVD) method (Waldhauser 2001). Detailed information for these clusters as well as the obtained uncertainties is shown in Table 2. The largest value of horizontal uncertainty is 0.56 km, while the largest value of vertical uncertainty is 0.87 km. Table S2 in Online Resource contains the catalog of the relocated events.

We also obtained precise relative locations by using cross-correlation differential times utilizing waveforms filtered between 1–10 Hz and 1–15 Hz. Filtering waveforms in this frequency range will result in smaller number of event pairs with cross-correlation coefficient of 0.7 or higher. This may be caused by strong wave

scattering effects of the short-wavelength component in higher frequencies which reduces the similarities of waveforms recorded by a particular station. The comparison of total number of event pairs obtained by cross-correlating lowpass filtered waveforms of 5 Hz and waveforms filtered between 1 and 10 Hz as well as 1–15 Hz are shown in Fig. S4 in Online Resource. Relative relocations by using cross-correlation differential times of waveforms filtered between 1–10 Hz and 1–15 Hz also result in smaller number of relocated events (2158 and 2159, respectively) with higher average RMS residuals (0.33 ± 0.36 s and 0.33 ± 0.37 s, respectively). The relative locations obtained by using cross-correlation differential times of waveforms filtered between 1–10 Hz and 1–15 Hz are shown in Fig. S6–S11 in Online Resource. Therefore, the use of lowpass filtered waveforms with corner frequency of 5 Hz is considered to be preferable. The relative locations we used for the subsequent analysis are the locations produced by using the mentioned filter. The obtained relative locations were subsequently plotted along with moment tensor solutions provided by NOA (Konstantinou et al. 2010) and RCMT (Pondrelli et al. 2002) as well as with the traces of known active faults in the SE Aegean contained in the GReDaSS database (Caputo and Pavlides 2013). In the next section, we present the most important features of the relocated seismicity.

5.2 Results

The most clustered seismicity in SE Aegean can be seen along the Gulf of Gökova (Fig. 6) and mainly concentrates in the northern part of the gulf. The most recent large earthquake in this area is the Bodrum-Kos earthquake that occurred near the island of Kara Ada. The mainshock was relocated at 36.9575°N and 27.4522°E at a depth of 11.3 km. Most of the earthquakes prior to

Table 2 Results of smaller clusters relocated using the SVD method to assess the relative relocation uncertainties. Neq is the number of events in each cluster; cLat, cLong, and cH represent centroid location of each cluster and depth, and ErrX ErrY ErrZ represent mean uncertainties

ID	Neq	cLat	cLong	cH (km)	ErrX (km)	ErrY (km)	ErrZ (km)
1	228	36.94	27.41	13.07	0.42	0.34	0.61
2	207	36.27	27.17	13.14	0.27	0.28	0.51
3	145	36.45	27.08	11.97	0.35	0.36	0.65
4	132	36.96	27.98	11.49	0.34	0.38	0.74
5	61	36.68	27.99	10.48	0.42	0.56	0.87
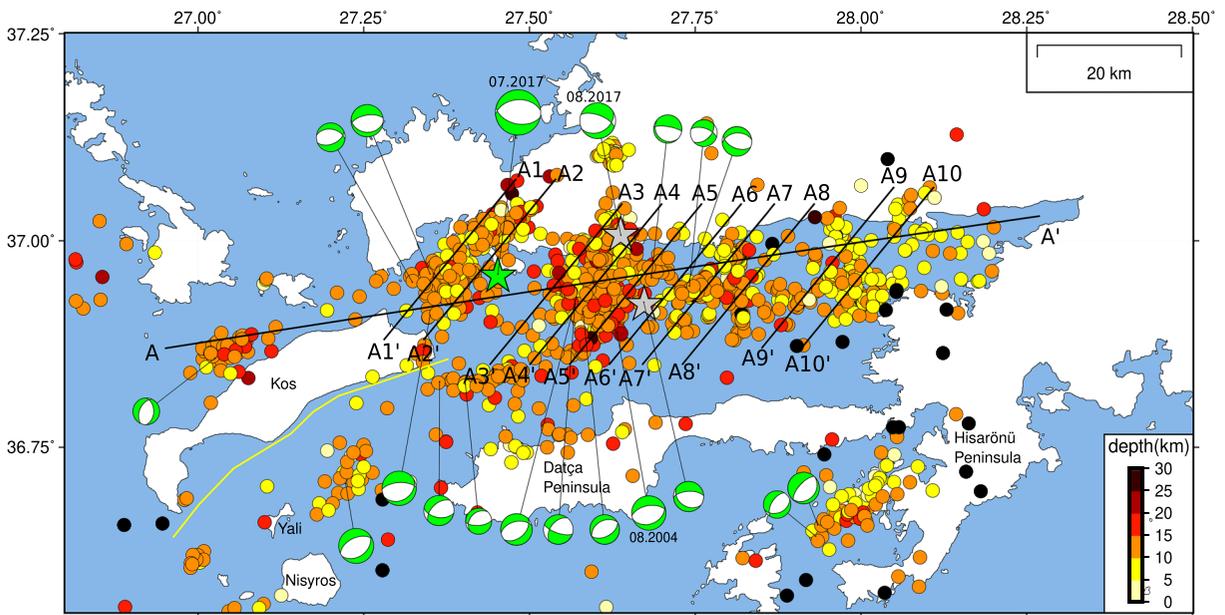
Fig. 6 Map showing relative locations of all the events that occurred in the Gulf of Gökova. The solid yellow lines represent active faults contained in the GReDaSS database (Caputo and Pavlides 2013). The color of every circle represents a depth value based on the scale at the lower right. Green star represents the epicenter of the Bodrum-Kos earthquake, while the epicenters of earthquakes with moment magnitude 5.0 or larger are shown as gray stars. The green beach balls show focal mechanisms of moderate and large earthquakes provided by NOA (Konstantinou et al. 2010) and RCMT (Pondrelli et al. 2002). The black lines represent the depth cross-sections

the Bodrum-Kos earthquake were concentrated in the north and far south of the mainshock. However, the aftershocks of Bodrum-Kos earthquake mostly occurred in the east and west of the mainshock (Fig. S12 in Online Resource). The epicentral distribution of the aftershocks formed an area that was almost free of any seismicity to the south of Kara Ada as shown in Fig. 6. This area is probably the asperity that ruptured during the mainshock of the mentioned earthquake. The aftershocks were mostly located shallower than 15 km as shown in the cross-section A–A' in Fig. 7. Even so, a small number of aftershocks can be found at depths deeper than 20 km. Cross-section A–A' shows an area almost free of seismicity located right above the mainshock that extends from very shallow depth down to about 11 km. This area indicates the most probable location of the slip patch of the Bodrum-Kos earthquake. Recent studies that combined InSAR, geodetic, and seismological data suggested that the slip patch of the Bodrum-Kos earthquake extends from a very shallow depth down to 12 km (Tiryakioğlu et al. 2018; Karasözen et al. 2018) which agrees well with our results. Depth cross-section A–A' also shows that the earthquakes located in the eastern part of the gulf have

shallower hypocentral depths. This observation is in agreement with the work of Tur et al. (2015) which shows decreasing depth of tectonic subsidence in the eastern part of the gulf.

The inversion of geodetic and InSAR data performed by Karasözen et al. (2018) and Ganas et al. (2019) showed that the fault that ruptured during the Bodrum-Kos earthquake was most probably a north-dipping normal fault. Our results in cross-sections A1–A1' to A10—A10' (Fig. 7) show no clear dipping direction for the mentioned fault. Even though the dipping direction is inconclusive, the length of the fault can still be determined. Based on the distribution of the aftershocks within the first week after the Bodrum-Kos earthquake, the length of the ruptured fault is 31 km with about ~ 20 km of it located to the east of the mainshock. From the seismicity distribution in cross-section A–A', the estimated total length of the fault located in the western to central part of the gulf is 50 km and some of it (~ 19 km), which we highlight as segment GF1, is still intact after the mainshock. Field data of Karasözen et al. (2018) suggested that there is also a separate fault segment located in the eastern part of the gulf, precisely along its northern boundary (segment GF2). The
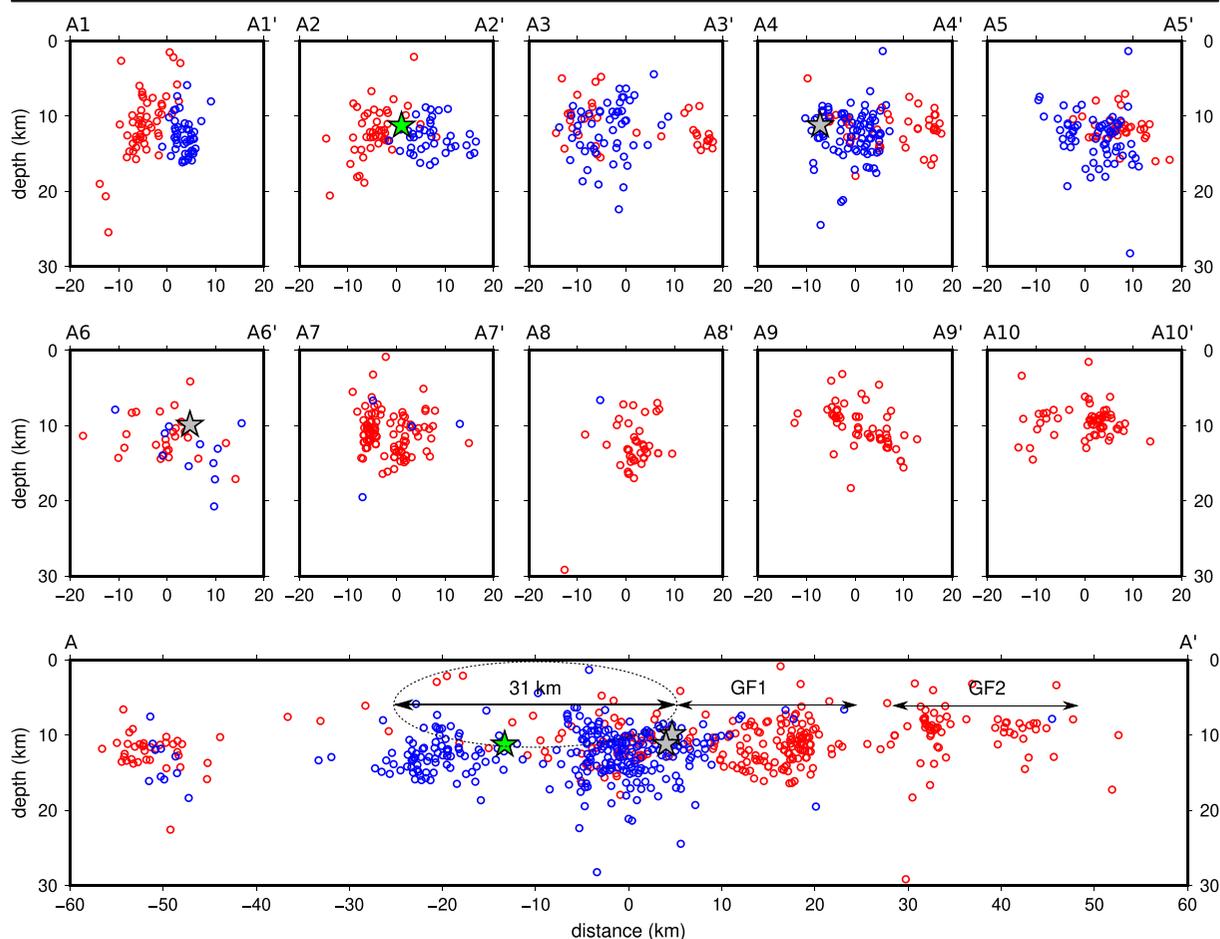
Fig. 7 Depth cross-sections corresponding to the profiles shown in Fig. 6. Red circles represent hypocenters of the earthquakes that occurred before the Bodrum-Kos earthquake, and blue circles show the earthquake hypocenters of the aftershocks. Dashed ellipse in cross-section A–A' denotes the most probable location of the slip patch that ruptured during the Bodrum-Kos earthquake. GF1 is the fault segment that did not rupture during the mainshock of Bodrum-Kos earthquake and GF2 is another fault segment observed in the field survey of Karasözen et al. (2018). All other symbols are the same as in Fig. 6

existence of GF2 is indicated by clustered shallow earthquakes in the eastern part of the gulf (Fig. 7). From the hypocentral distribution of these earthquakes shown in cross-sections A9–A9' and A10–A10', we cannot infer whether GF2 is a north-dipping or south-dipping fault. Nevertheless, we also estimated the length of GF2 by using the seismicity distribution, which yielded a length of 20 km.

A smaller cluster of earthquakes can be observed in the SW of Nisyros caldera also extending to the west of Tilos island (Fig. 8). The relocated hypocenters of these earthquakes are distributed from shallow depth down to about 20 km. The local magnitudes of the earthquakes in this cluster vary from 1.6 to 3.9 as determined by NOA. It should be noted that this

cluster does not coincide with any of the active faults contained in the GReDaSS database. It seems likely that this cluster may have been caused by the reactivation of an offshore fault, considering that swath bathymetry SW of Nisyros indicates the existence of extensive seafloor faulting (Piper and Perissoratis 2003). This argument is further strengthened by the ISC-GEM location of 5 December 1968 earthquake with moment magnitude 6.1 that is close to the location of this cluster. Past earthquake activity that was located near Nisyros occurred on its NW coast during the 1995–1997 unrest (Sachpazi et al. 2002). Inflation of a magma chamber at the mentioned location was suggested as the most likely cause for the intense seismicity during this period. Our relocation results

Fig. 8 Map showing the relative locations for the area of Nisyros. Dashed red lines outline the dipping of the delineated fault planes. All other symbols are the same as in Fig. 6
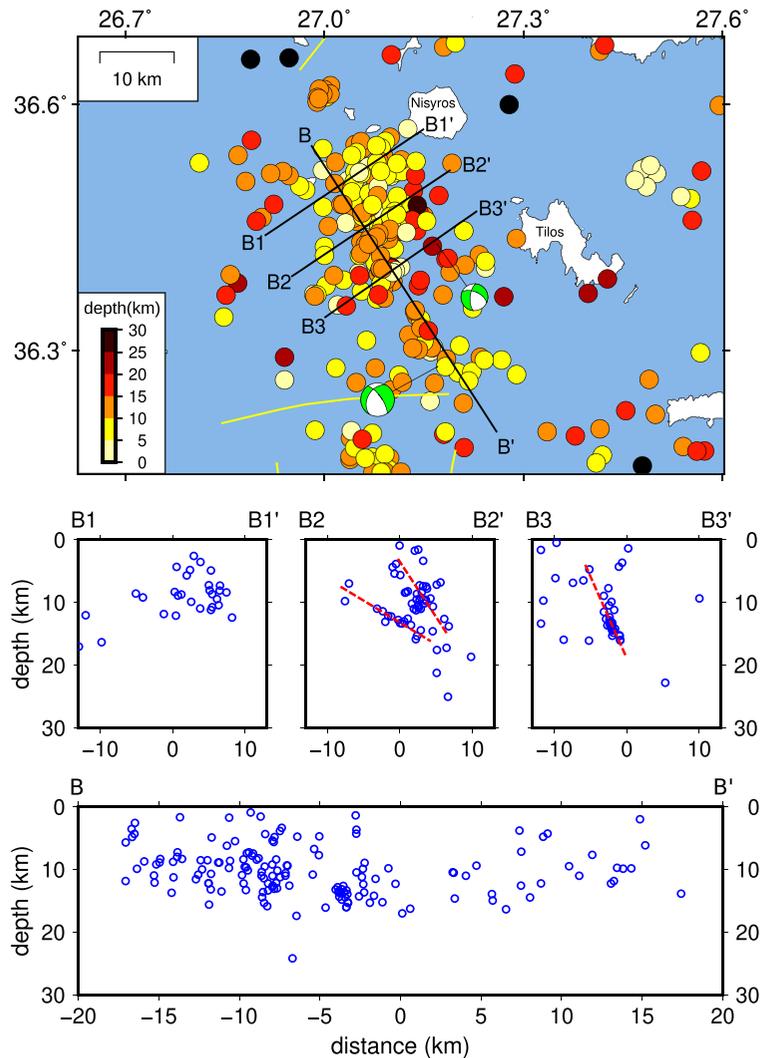
show no such cluster in this area during the different periods covered by our study.

Two other earthquake clusters are located near Karpathos island (Fig. 9). The first cluster is located to the NW of Karpathos and coincides with a fault contained in the GReDaSS database, namely the fault KAF1. The earthquakes in this cluster have various hypocentral depths from 10 to 25 km. The moment tensor solutions indicate that the seismicity of this cluster occurred as a result of normal faulting with a dipping angle of 38–67°. The hypocentral distribution in cross-section C2–C2', however, shows that KAF1 is steep with unclear dipping direction. The relocated seismicity in this area appears to be distributed to the east of the mentioned fault, suggesting that KAF1 may be dipping to the east. The other earthquake cluster can be found

exactly to the north of Karpathos island. This cluster occurred very close to a fault contained in the GReDaSS database, referred to as KAF2. However, it is unlikely that this mentioned earthquake cluster is related to this fault. Tur et al. (2015) used seismic-reflection profiles, GPS slip vectors, and available fault-plane solutions to investigate the subsided bathymetry known as the Gökova-Nisyros-Karpathos Graben that extends from the Gulf of Gökova to the west of Karpathos. It is possible that KAF2 is outlining the western boundary of this graben and is dipping to the west, uplifting the western coast of Karpathos as a result. The GReDaSS database also specifies that this fault is steeply dipping to the west with a dipping angle of 70–89°. There is no significant seismicity along KAF2 during our period of study, making it impossible to infer its dipping direction.
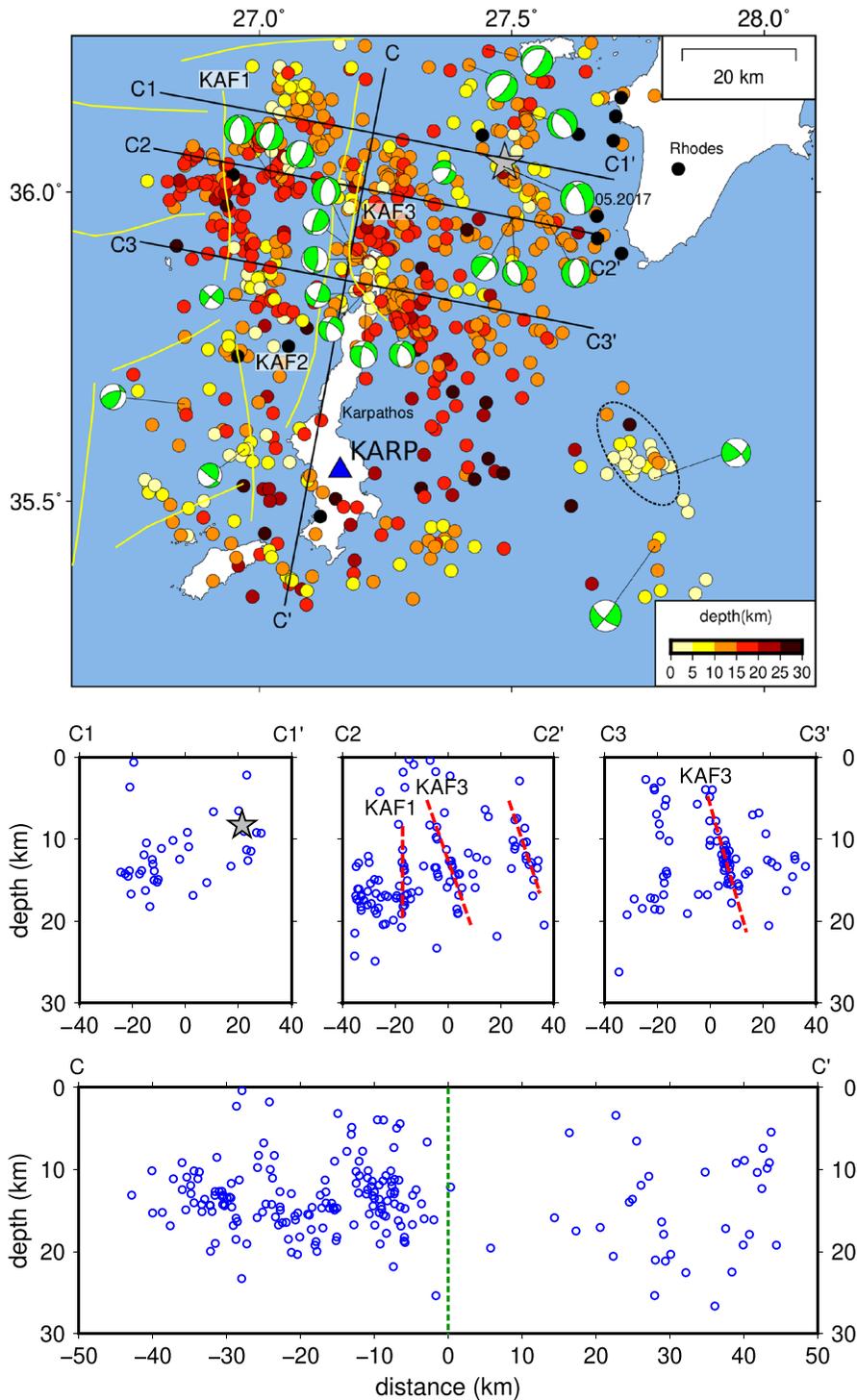
Fig. 9 Relative locations of earthquakes in the southern part of the study area. The dashed black ellipse represents an unconstrained earthquake cluster located in an area lacking station coverage. KAF1 and KAF3 are the seismically active faults in this area, while KAF2 is a fault contained in GReDaSS database that exhibited no seismicity during our period of study. Dashed green line in the cross-section C–C' denotes the boundary of well-constrained events and the diffuse locations in the south of Karpathos. All other symbols are the same as in Fig. 6

The hypocentral distribution in cross-sections C2–C2' and C3–C3' as well as the available moment tensor solutions reveal that the earthquake cluster north of Karpathos was generated by an east-dipping normal fault with a dipping angle of 46–58° (KAF3). Based on the epicentral distribution of the mentioned earthquake cluster, we inferred that KAF3 may be located 3–5 km to the east of KAF2. Although it has been seismically active during the different periods of our study, KAF3 is not contained in the GReDaSS database.

From the depth cross-section C–C' of Fig. 9, we can clearly see that some of the hypocentral depths of the earthquakes that occurred in the northern part of this area appear more clustered, while the rest of the events in the southern part exhibit more diffuse distribution. The boundary between these two groups of events is also very distinguishable (the green line in cross-section C–C' of Fig. 9). This difference may be caused by the lack of azimuthal coverage in this part of the SE Aegean and due to large epicentral distances of up to 20 km or more between these events and station KARP which is the closest station in the area. A small earthquake cluster, marked with a dashed ellipse in Fig. 9, can also be seen about 40 km to the east of Karpathos. This cluster is elongated in NW-SE direction and consists mostly of earthquakes with hypocentral depths of less than 10 km. It is important to note that there is no seismic station located SE from this cluster, while the closest station is KARP which is about 57 km to the west. In addition, most faults along the plate boundary in this area have NE-SW orientation, exactly perpendicular to the orientation of the mentioned cluster (Özbakır et al. 2013). The lack of constraint in the SE direction together with the NE-SW orientation of the faults in the area strengthen the possibility that the orientation of this cluster is most likely an artifact and that the relative locations obtained are not well constrained.

6 Delineated faults and expected earthquake magnitudes

The relationship between seismicity and active faults in SE Aegean can be examined by utilizing the precise locations of all the earthquakes that occurred in our study area. Fig. 10 shows all the active faults in the SE Aegean included in the GReDaSS database (Caputo and Pavlides 2013) as well as faults exhibiting seismicity during our period of study. Location of moderate to large earthquakes obtained from the ISC-GEM catalog (Storchak et al. 2013) and their error ellipses are also overlain in Fig. 10 as well as the epicenter of the 2017 Bodrum-Kos earthquake. Furthermore, the Figure also shows σ_3-axes orientation from the present-day stress field of the Aegean that has been derived by Konstantinou et al. (2016) along a grid with 0.35° node spacing. The orientation of the σ_3-axes in Fig. 10 shows a counterclockwise rotation from NNW-SSE in the north to almost E-W in the south of our study area and with plunge angles varying between 0.04 and 7.03° from north to south. As it can be seen in the figure, the faults that were seismically active during the period of our study are the ones whose strikes are almost perpendicular to the σ_3-axes orientation, which are the faults with ENE-WSW strike in the area north of Tilos and N-S strike in the area south of Tilos. On the other hand, faults with a strike parallel to the orientation of σ_3-axes experience extension along strike, resulting in no seismicity. The dominant structures in SE Aegean range from normal faulting in the Gulf of Gökova, Nisyros, and the offshore area around Tilos, to oblique dip-slip in the island of Karpathos to the south.

The distribution of hypocenters obtained from the precise relative locations can be used to infer the thickness of the seismogenic layer in our study area. Considering that the magnitude of an earthquake does not depend only on the length of a ruptured fault but also on its width, inferring the thickness of the seismogenic layer becomes important. By using the value of seismogenic layer thickness H, we will be able to estimate the fault width as $W = H/\sin\delta$, where δ is the dip of the fault. The ruptured area A is then obtained by multiplying the value of fault length L with the estimated fault width W. Finally, we calculated the expected moment magnitudes along several faults by utilizing the scaling relationships developed by Konstantinou (2014) that state that the moment magnitude M of an earthquake with rupture area A is

$$M = \log A + 3.82, \quad \text{if } A \leq 251 \text{ km}^2 \qquad (1)$$

$$M = \frac{4}{3}\log A + 3.07, \quad \text{if } A > 251 \text{ km}^2 \qquad (2)$$

In this study, we calculated the fault length from the extent of the seismicity. In order to determine the dip of each fault, we matched the nodal planes of the available moment tensor solutions with the obtained cross-
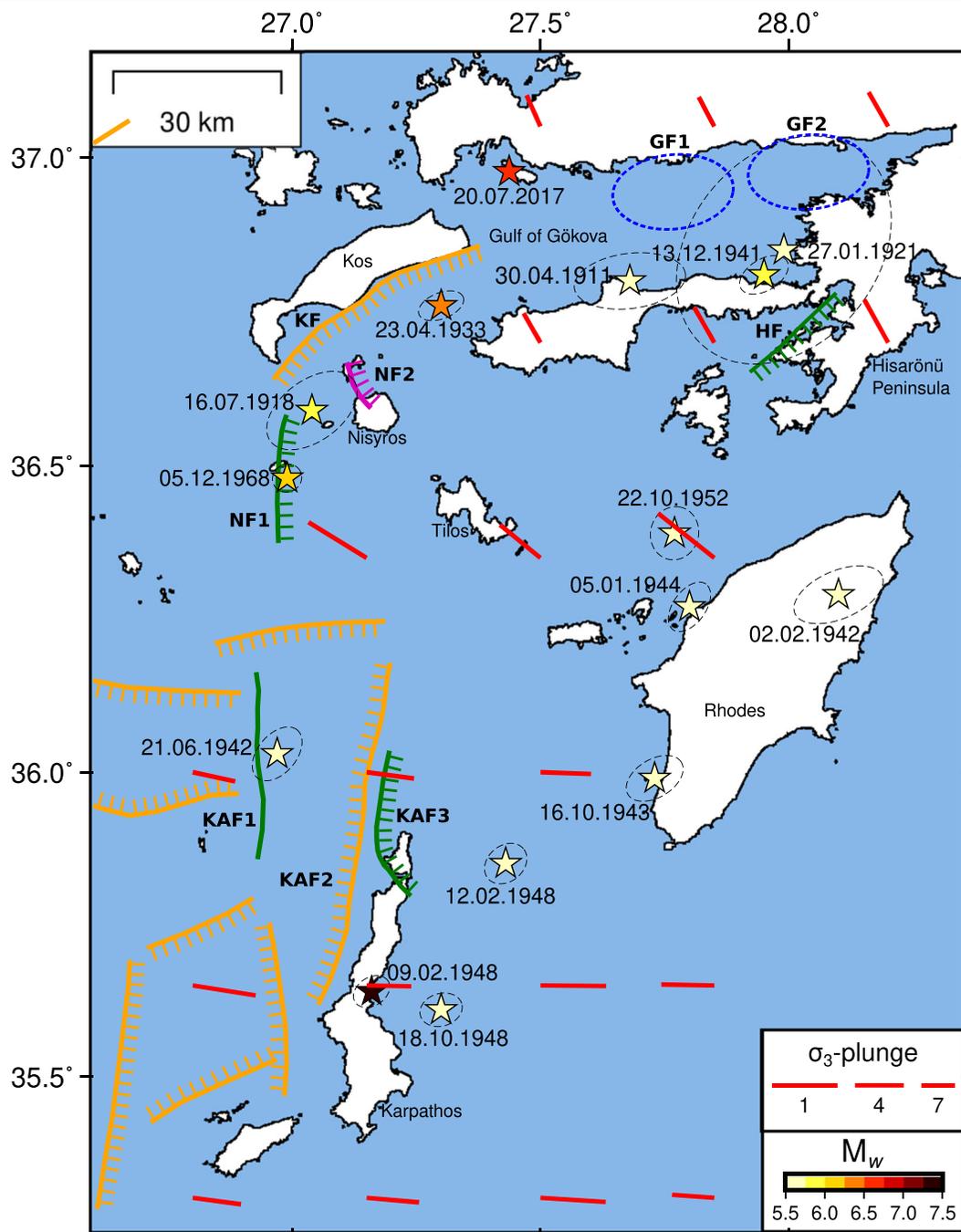
Fig. 10 Map showing σ₃-axes orientation across SE Aegean (red solid lines) adopted from Konstantinou et al. (2016). The length of each red solid line represents σ₃ axes plunge shown on the scale at the lower right. Solid orange lines show active faults from the GReDaSS database (Caputo and Pavlides 2013). Solid green lines represent faults with seismicity delineated in this study. Comb-like lines show the direction of fault dipping. The magenta line extending from NW Nisyros to Yali shows the active fault zone investigated by Nomikou and Papanikolaou (2011). The stars represent moderate to large events from 1911 to 1968 taken from the ISC-GEM catalog (Storchak et al. 2013). The color of every star indicates a moment magnitude based on the scale at the lower right. The dashed ellipses indicate the error ellipse of each earthquake location. The blue dashed ellipses show the most probable location of fault segments in the Gulf of Gökova.

sections to infer which nodal plane is following the dip direction of the relocated earthquakes. The seismogenic layer thickness itself can be estimated by using the 5th and 95th percentile for each hypocentral depth distribution as the onset and cutoff depths, respectively. Figure 11 shows the thickness of seismogenic layers in the areas with high seismicity, such as the Gulf of Gökova, Nisyros, and Karpathos. For the area of Karpathos, we only included hypocentral depths of well-constrained events (i.e., to the north of station KARP). We found that the seismogenic layer thickness for the Gulf of Gökova and its surrounding area is 12.1 km, while for the areas of Nisyros and Karpathos, the seismogenic layer thickness is 12.9 km and 15.4 km, respectively. By comparison, Konstantinou (2018) found that NE Aegean has a somewhat thicker seismogenic layer of 14.8–15.8 km. Thicker seismogenic layer in an area makes it more prone to the nucleation of a large earthquake. This fact has to be considered in future assessments of seismic hazard in the SE Aegean, especially for the area of Karpathos.

There are at least eight faults within our study area that may rupture and cause large earthquakes in the future (cf. Fig. 10). These faults are the two fault segments in the Gulf of Gökova (GF1 and GF2), the Kos Fault (KF) located along the southern coast of Kos island, a fault extending from NE to SW in the Hisarönü Peninsula (HF), the fault located to the west of Nisyros (NF1), the active fault located far NW of Karpathos (KAF1), and the fault north of Karpathos (KAF3). Some of these faults ruptured in the past and generated moderate to large earthquakes as summarized previously in Table 1. Furthermore, we also calculated the expected magnitude along an east-dipping fault that extends from the north-western part of Nisyros to the small island of Yali (NF2) and was previously studied by Nomikou and Papanikolaou (2011). For this fault, we took the length and its dipping angle directly from the mentioned study. The geometrical properties of all faults, as well as the expected magnitude for each of them, are summarized in Table 3.

6.1 Gulf of Gökova and Kos

We estimated the expected magnitude for fault segment GF1 with a length of 19 km, located in the center of the Gulf of Gökova, which is shown in cross-section A–A' of Fig. 7. In order to determine the dip of the mentioned fault segment, we took the median dip of nodal planes of
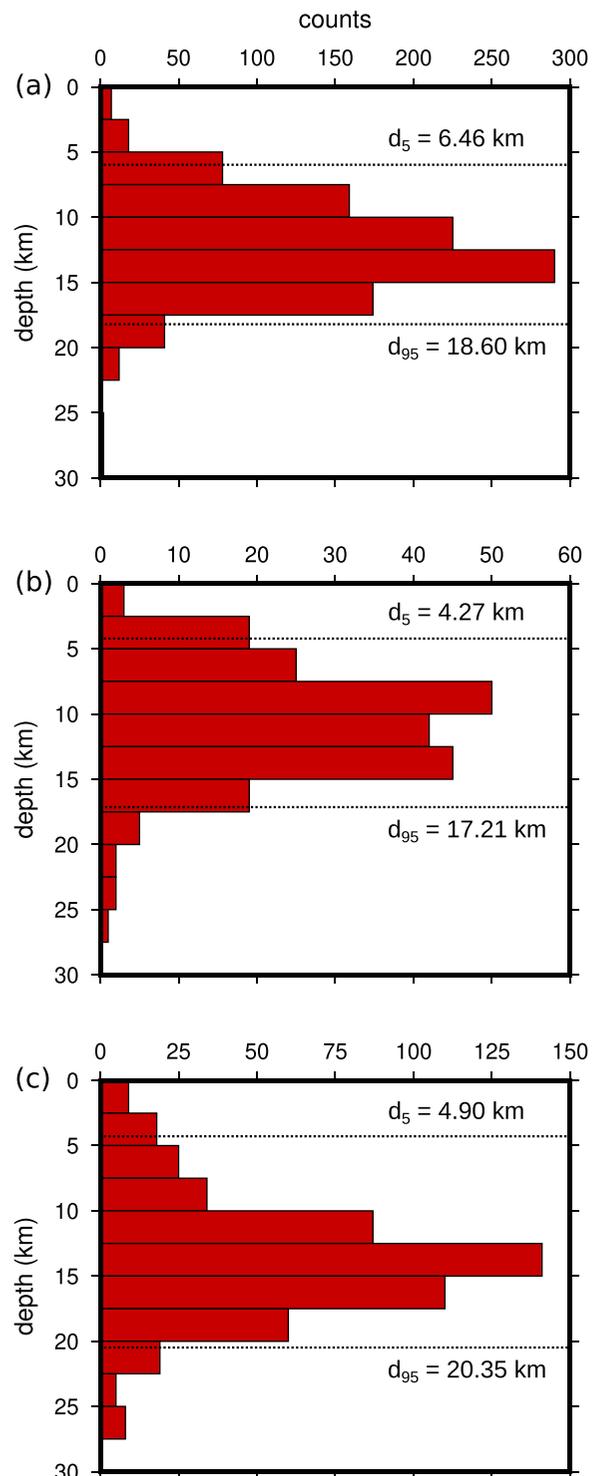
Fig. 11 Histograms showing hypocentral depth distribution of relocated events that occurred around: (**a**) Gulf of Gökova, (**b**) Nisyros island, and (**c**) Karpathos and its surrounding area. The 5th and 95th percentile in each depth distribution are shown by symbols d_5 and d_{95}, respectively.

Table 3 Geometrical properties of the faults in the study area that may produce large earthquakes in the future. H is the seismogenic layer thickness of the area, L is the fault length, δ is the dipping angle, W is the width of the fault, A is the rupture area, and M is the expected moment magnitude

Fault	H (km)	L (km)	δ	W (km)	A (km^2)	M
GF1	12.1	19	43°	17.8	338	6.4
GF2	12.1	20	43°	17.7	355	6.5
HF	12.1	15	62°	13.8	207	6.1
KF	12.1	45	51°	15.6	701	6.9
NF1 (scenario 1)	12.9	20	46°	17.9	359	6.5
NF1 (scenario 2)	12.9	20	66°	14.1	282	6.3
NF2	12.9	9	75°	14.4	120	5.9
KAF1	15.4	33	65°	17.0	561	6.7
KAF3	15.4	30	53°	19.3	578	6.8

the available moment tensor solutions from NOA and other agencies (GCMT, GFZ, USGS, KOERI, INGV, and AUTH). The north-dipping nodal planes from all the obtained moment tensor solutions lie between 39 and 56° with a median of 43°, while the south-dipping nodal planes range between 35 and 54° with a median of 50°. Since the dipping direction of the mentioned fault is not clear, we consider that the fault is dipping to the north following the results of geodetic and InSAR data inversions published by Karasözen et al. (2018) and Ganas et al. (2019). We then used the median of the north-dipping nodal planes in the calculation, yielding an expected magnitude of 6.4. It is important to note that the use of median of the south-dipping nodal planes in the calculation will only yield 0.06 units of discrepancy in the resulting expected magnitude. We also estimated expected magnitude for GF2 that is located in the eastern part of the gulf with a length of 20 km. The extent of seismicity indicating GF2 can be observed in cross-section A–A' in Fig. 7. There are no moment tensor solutions available for the earthquakes that occurred in the eastern part of the gulf; therefore, we used the same dip angle value of 43° for GF2 and obtained the expected magnitude of 6.5. Although GF2 is located in close proximity to GF1, it is a completely separate fault segment (see Karasözen et al. 2018) located less than 10 km to the east of GF1. A cluster of earthquakes can also be observed to the south of Gulf of Gökova, outlining a fault that may produce a large earthquake in the Hisarönü Peninsula (HF). A large portion of HF is contained within the error ellipse of the earthquake that occurred on 27 January 1921, indicating that this earthquake might be related to HF. The fault dip determined

from the available moment tensor solutions and depth cross-section (Fig. S13 in Online Resource) is 62°. Combining this fault dip with the fault length of HF (~ 15 km) and the seismogenic layer thickness of this particular area, we obtained an expected moment magnitude of 6.1 which is considerably higher when compared to the moment magnitude of the 1921 earthquake (M_w 5.5 ± 0.20). On the other hand, we also calculated the expected magnitude of a future earthquake for the fault KF. The lack of significant seismicity along this fault during the different periods covered by our study leads to the possibility that it either exhibits aseismic creep or that it is locked and is accumulating strain energy. KF itself is a normal fault that likely produced the Kos earthquake on 23 April 1933 (M_w 6.4 ± 0.32). Assuming that the entire fault ruptures, the expected moment magnitude will be 6.9 which is higher than the moment magnitude of the 1933 Kos earthquake even if we take into account the magnitude uncertainty.

6.2 Nisyros-Yali

We found two major normal faults in Nisyros island and its surrounding area that may generate large earthquakes in the future. NF1 is the fault that might have caused two large earthquakes on 5 December 1968 (M_w 6.1 ± 0.30) and 16 July 1918 (M_w 5.9 ±0.42). Cross-section B2–B2' of Fig. 8 shows structures similar to two faults that dip eastward with different dipping angle. Therefore, we considered two scenarios involving different dipping angles in order to estimate the expected magnitude for this fault. In the first scenario, we used the focal mechanism of the earthquake on 5 December 1968, derived

by McKenzie (1972), that shows a fault plane with dipping angle of 46°. By using this value and taking the extent of the seismicity SW of Nisyros as the fault length (~ 20 km), we calculated the expected moment magnitude and obtained a value of 6.5. As a second scenario, we consider a steeper dip of 66° as shown in cross-section B2–B2', yielding an expected magnitude of 6.3. The expected magnitude of the second scenario falls in the ranges of magnitude uncertainties for both 1968 and 1918 earthquake. This indicates the possibility that NF1 has a very steep dip of ~ 66°. Another major fault in this area is NF2 with a length of 9 km extending from NW part of Nisyros to the small island of Yali with a steep dipping angle of 75°. Nomikou and Papanikolaou (2011) also calculated expected magnitudes for this fault by using the relationships developed by Wells and Coppersmith (1994) and Pavlides and Caputo (2004), yielding values that ranged from 6.1 to 6.3. However, if we assume that this fault ruptures completely along its length, we estimate that the expected moment magnitude will have a lower value of 5.9. The difference in expected magnitudes from both calculations is probably caused by the use of relationships by Nomikou and Papanikolaou (2011) that take only fault length into account, whereas our calculation utilized both fault length and width.

6.3 Karpathos

Two seismically active faults are located in the Karpathos area, namely KAF1 and KAF3. From the available moment tensor solutions and epicentral distribution in this area (Fig. 9) we can infer that KAF1 is a normal fault which dips to the east. The error ellipse of the ISC-GEM catalog suggests that this fault might be related to a moderate earthquake that occurred on 21 June 1942 (M_w 5.5 ± 0.20). The nodal planes of the available moment tensor solutions for earthquakes that occurred along this fault show that it has a dipping angle of 65°. The resulting expected magnitude for KAF1 is 6.7, which is considerably higher than the magnitude of the 1942 earthquake. The other active fault in this area is KAF3 with a fault dip of 53° to the east. We estimated the length of KAF3 based on the extent of the seismicity north of Karpathos (~ 30 km) and calculated the expected magnitude, yielding a value of 6.8. Another fault in this area that is contained in the GReDaSS database is KAF2. This fault has been seismically silent during our period of study and the information regarding its

properties can only be found in the GReDaSS database. If we use these geometrical properties and calculate the expected magnitude, KAF2 may generate a crustal earthquake with a magnitude in the order of 7.0.

A large earthquake of moment magnitude 7.3 (± 0.20) occurred on 9 February 1948 in close proximity to KAF2 (~ 10 km). This earthquake was reassessed by Ebelling et al. (2012) by using digitized historical seismograms recorded by 108 stations with epicentral distances up to 100°. According to their study, the hypocenter of the 1948 earthquake was located at 60 km depth with 10–15 km vertical error. Such a large depth suggests that this earthquake is probably related to the subduction process between the African and Aegean plates. Moreover, the moment tensor of this earthquake also showed a thrust-dominated solution with E-W strike, which is incompatible with the N-S striking KAF2. Therefore, we conclude that the 1948 earthquake is likely not related to KAF2 and that there was no other large crustal earthquake since 1911 in the ISC-GEM catalog that may be related to this fault. Since Karpathos exhibits relatively large expected moment magnitudes in SE Aegean and is also exposed to tsunami hazards, continuous monitoring as well as further studies on the seismicity of the faults in this area are required.

7 Conclusions

Our study focused on the seismicity of the SE Aegean recorded during the periods of October 2005 to March 2007 and from January 2011 to June 2018, including the crustal earthquakes that occurred in the Gulf of Gökova during the period of August 2004 to January 2005 and moderate events from March 2006 to November 2010. These events were used to derive a minimum 1D model with station delays, which later was utilized to obtain absolute and precise relative locations. Active faults in the area were then delineated by using these precise locations. The conclusions of our work are as follows:

1. As many as 3055 events were successfully located by using probabilistic nonlinear location algorithm NLLOC and the newly derived minimum 1D model with station delays. Both the average horizontal and vertical uncertainties of these absolute locations were less than 6.0 km with average RMS residual of 0.35 s. Differences in RMS residual and depth

distributions were found in the comparison between the obtained absolute locations and the NOA routine locations. These differences were partly caused by the use of a relatively simple velocity model by NOA.

2. Precise relative locations of 2200 events were obtained by using the double-difference method with less than 1.0 km vertical and horizontal uncertainties. These relative locations were used to delineate the fault segments along the Gulf of Gökova and also the fault outlined by a cluster of earthquakes SW of Nisyros. Two active faults in Karpathos area were also delineated. However, the depths of the events located south of seismic station KARP were not well constrained due to the lack of azimuthal coverage and also due to large distances between these events and the closest seismic station.

3. The comparison of the resulting seismicity distribution and the active faults of the study area with the regional stress field shows that seismicity was only observed along faults with ENE-WSW strike in the area north of Tilos and N-S strike in the area south of Tilos. The seismotectonic regime in SE Aegean varies from normal faulting in the areas of Gulf of Gökova, Nisyros, and Tilos to oblique dip-slip in the island of Karpathos to the south.

4. The seismogenic layer thickness in the SE Aegean derived from the value difference between the 5th and 95th percentile of the hypocentral depth distribution is ranging from 12.1 to 15.4 km. Based on this thickness and the geometrical properties of faults in the area, the expected moment magnitudes of potential earthquakes vary between 5.9 and 6.9. Kos Fault (KF), which exhibited lack of significant seismicity during different periods of our study has the potential to produce the largest earthquake in SE Aegean with moment magnitude equal to 6.9. Since most of these faults lie offshore, there is an increased probability that a large crustal earthquake will be followed by a tsunami. It is therefore of particular importance to closely monitor the seismicity in Southern Aegean and strengthen the existing tsunami early warning capabilities.

Compliance with ethical standards

References

Boğaziçi University Kandilli Observatory and Earthquake Research Institute (2001) Boğaziçi University Kandilli Observatory and Earthquake Research Institute. International Federation of Digital Seismograph Networks Dataset/Seismic Network, https://doi.org/10.7914/SN/KO

Bohnhoff M, Harjes HP, Meier T (2005) Deformation and stress regimes in the Hellenic subduction zone from focal mechanisms. J Seismol 9(3):341–366. https://doi.org/10.1007/s10950-005-8720-5

Brüstle A (2012) Seismicity of the eastern Hellenic Subduction Zone. Ph.D. thesis, Ruhr University, Bochum

Caputo R, Pavlides S (2013) The Greek Database of Seismogenic Sources (GreDaSS), Version 2.0.0: a compilation of potential seismogenic sources (Mw & 5.5) in the Aegean Region. https://doi.org/10.15160/unife/gredass/0200. http://gredass.unife.it/.

Ebeling CW, Okal EA, Kalligeris N, Synolakis CE (2012) Modern seismological reassessment and tsunami simulation of historical Hellenic Arc earthquakes. Tectonophysics 530–531:225–239. https://doi.org/10.1016/j.tecto.2011.12.036

Font Y, Kao H, Lallemand S, Liu CS, Chiao LY (2004) Hypocenter determination offshore of eastern Taiwan using the maximum intersection method. Geophys J Int 158:655–675. https://doi.org/10.1111/j.1365-246X.2004.02317.x

Friederich W, Meier T (2005) EGELADOS project 2005/07, RUB Bochum, Germany. Deutsches GeoForschungsZentrum GFZ. https://doi.org/10.14470/m87550267382

Ganas A, Elias P, Kapetanidis V, Valkaniotis S, Briole P, Kassaras I, Argyrakis P, Barberopoulou A, Moshou A (2019) The July 20, 2017 M6.6 Kos Earthquake: seismic and geodetic evidence for an active north-dipping normal fault at the

western end of the Gulf of Gökova (SE Aegean Sea). Pure Appl Geophys. https://doi.org/10.1007/s00024-019-02154-y

Hall J, Aksu AE, Yaltırak C, Winsor JD (2009) Structural architecture of the Rhodes Basin: a deep depocentre that evolved since the Pliocene at the junction of Hellenic and Cyprus Arcs, eastern Mediterranean. Mar Geol 258:1–23. https://doi.org/10.1016/j.margeo.2008.02.007

Hollenstein C, Müller MD, Geiger A, Kahle H-G (2008) Crustal motion and deformation in Greece from a decade of GPS measurements, 1993–2003. Tectonophysics 449(1):17–40. https://doi.org/10.1016/j.tecto.2007.12.006

Karagianni EE, Papazachos CB, Panagiotopoulos DG, Suhaldoc P, Vuan A, Panza GF (2005) Shear velocity structure in the Aegean area obtained by inversion of Rayleigh waves. Geophis J Int 160:127–143. https://doi.org/10.1111/j.1365-246X.2005.02354.x

Karasözen E, Nissen E, Büyükakpınar P, Musavver SC, Kahraman M, Kalkan Ertan E, Abgarmi B, Ghods A, Özacar A (2018) The 20 July 2017 Mw 6.6 Bodrum–Kos earthquake illuminates active faulting in the Gulf of Gökova, SW Turkey. Geophys J Int 214. https://doi.org/10.1093/gji/ggy114

Kissling E, Ellsworth WL, Eberhart-Phillips D, Kradolfer U (1994) Initial reference models in local earthquake tomography. J Geophys Res 99:19 635–19 646

Konstantinou KI (2014) Moment magnitude–rupture area scaling and stress-drop variations for earthquakes in the Mediterranean Region. Bull Seismol Soc Am 104:5. https://doi.org/10.1785/0120140062

Konstantinou KI (2017) Accurate relocation of seismicity along the North Aegean Trough and its relation to active tectonics. Tectonophysics 717:372–382. https://doi.org/10.1016/j.tecto.2017.08.021

Konstantinou KI (2018) Estimation of optimum velocity model and precise earthquake locations in NE Aegean: implications for seismotectonics and seismic hazard. J Geodyn 121:143–154. https://doi.org/10.1016/j.jog.2018.07.005

Konstantinou KI, Melis NS, Boukouras K (2010) Routine regional moment tensor inversion for earthquakes in the Greek region: the National Observatory of Athens (NOA) Database (2001–2006). Seismol Res Lett 81:750–760. https://doi.org/10.1785/gssrl.81.5.750

Konstantinou KI, Mouslopoulou V, Liang W-T, Heidbach O, Oncken O, Suppe J (2016) Present-day crustal stress field in Greece inferred from regional-scale damped inversion of earthquake focal mechanisms. J. Geophys. Res. Solid Earth 122:506–523. https://doi.org/10.1002/2016JB013272

Kurt H, Demirbağ E, Kuşçu İ (1999) Investigation of the submarine active tectonism in the Gökova gulf, southwest Anatolia–southeast Aegean Sea, by multi-channel seismic reflection data. Tectonophysics 305(4):477–496. https://doi.org/10.1016/S0040-1951(99)00037-2

Lomax A, Curtis A (2001) Fast, probabilistic earthquake location in 3D models using Oct-Tree importance sampling. Geophys Res Abstr 3

Lomax A, Virieux J, Volcant P, Thierry-Berge C (2000) Probabilistic earthquake location in 3D and layered models, In Advances is seismic events location. 101-134 pp. Thurber, C. H., Rabinowitz, N. (eds), Amsterdam

Maleki V, Hossein Shomali Z, Hatami MR, Pakzad M, Lomax A (2013) Earthquake relocation in the central Alborz region of

Iran using a nonlinear probabilistic method. J Seismol 17: 615–628. https://doi.org/10.1007/s10950-012-9342-3

McClusky S, Balassanian S, Barka A, Demir C, Ergintav S, Georgiev I, Gurkan O, Hamburger M, Hurst K, Kahle H, Kastens K, Kekelidze G, King R, Kotzev V, Lenk O, Mahmoud S, Mishin A, Nadariya M, Ouzounis A, Paradissis D, Peter Y, Prilepin M, Reilinger R, Sanli I, Seeger H, Tealeb A, Toksöz MN, Veis G (2000) Global positioning system constraints on plate kinematic and dynamics in the eastern Mediterranean and Caucasus. J Geophys Res 105:5695–5719. https://doi.org/10.1029/1999JB900351

McKenzie D (1972) Active tectonics of the Mediterranean Region. Geophys J Roy Astr S 30:109–185. https://doi.org/10.1111/j.1365-246X.1972.tb02351.x

National Observatory of Athens, Institute of Geodynamics, Athens (1997) National Observatory of Athens Seismic Network. International Federation of Digital Seismograph Networks Dataset/Seismic Network https://doi.org/10.7914/SN/HL

Nomikou P, Papanikolaou D (2011) Extension of active fault zones on Nisyros volcano across the Yali-Nisyros Channel based on onshore and offshore data. Mar Geophys Res 32: 181–192. https://doi.org/10.1007/s11001-011-9119-z

Nyst M, Thatcher W (2004) New constraints on the active tectonic deformation of the Aegean. J Geophys Res 109:B11406. https://doi.org/10.1029/2003JB002830

Özbakır AD, Şengör AMC, Wortel MJR, Govers R (2013) The Pliny–Strabo trench region: a large shear zone resulting from slab tearing. Earth Planet Sci Lett 375:188–195. https://doi.org/10.1016/j.epsl.2013.05.025

Papazachos BC, Papazachou C (2003) The earthquakes of Greece. Ziti Publications, Thessaloniki, p 317

Papazachos BC, Karakostas VG, Papazachos CB, Scordilis EM (2000) The geometry of the Wadati–Benioff zone and lithospheric kinematics in the Hellenic arc. Tectonophysics 319(4):275–300. https://doi.org/10.1016/S0040-1951(99)00299-1

Pavlides S, Caputo R (2004) Magnitude versus faults' surface parameters: quantitative relationships from the Aegean Region. Tectonophysics 380(3-4):159–188. https://doi.org/10.1016/j.tecto.2003.09.019

Piper, D. J. W., Perissoratis, C., (2003). Quaternary neotectonics of the South Aegean arc. Mar Geol, 198, 259-288, https://doi.org/10.1016/S0025-3227(03)00118-X

Podvin P, Lecomte I (1991) Finite difference computation of traveltimes in very contrasted velocity models: a massively parallel approach and its associated tools. Geophys J Int 105: 271–284

Pondrelli S, Morelli A, Ekström G, Mazza S, Boschi E, Dziewonski AM (2002) European-Mediterranean regional centroid-moment tensors: 1997-2000. Phys Earth Planet Inter 130:71–101. https://doi.org/10.1016/j.pepi.2011.01.007

Reilinger R, McClusky S, Vernant P, Lawrence S, Ergintav S, Cakmak R, Ozener H, Kadirov F, Guliev I, Stepanyan R, Nadariya M, Hahubia G, Mahmoud S, Sakr K, ArRajehi A, Paradissis D, Al-Aydrus A, Prilepin M, Guseva T, Evren E, Dmitrotsa A, Filikov SV, Gomez F, Al-Ghazzi R, Karam G (2006) GPS constraints on continental deforma-tion in the Africa–Arabia–Eurasia continental collision zone and implications for thedynamics of plate interactions. J Geophys Res 111. https://doi.org/10.1029/2005JB004051

Reilinger R, McClusky S, Paradisis D, Ergintav S, Vernant P (2010) Geodetic constraints on the tectonic evolution of the Aegean region and strain accumulation along the Hellenic subduction zone. Tectonophysics 488:22–30. https://doi.org/10.1016/j.tecto.2009.05.027

Rontogianni S (2010) Comparison of geodetic and seismic strain rates in Greece by using a uniform processing approach to campaign GPS measurements over the interval 1994–2000. J Geodyn 50:381–399. https://doi.org/10.1016/j.jog.2010.04.008

Sachpazi M, Kontoes C, Voulgaris N, Laigle M, Vougioukalakis G, Sikioti O, Stavrakakis G, Baskoutas J, Kalogeras J, Lepine JC (2002) Seismological and SAR signature of unrest at Nisyros caldera. Greece J Volc Geotherm 116:19–33. https://doi.org/10.1016/S0377-0273(01)00334-1

Sodoudi F, Kind R, Hatzfeld D, Priestley K, Hanka W, Wylegalla K, Stavrakakis G, Vafidis A, Harjes H-P, Bohnhoff M (2006) Lithospheric structure of the Aegean obtained from P and S receiver functions. J Geophys Res 111:B12307. https://doi.org/10.1029/2005JB003932

Storchak DA, Di Giacomo D, Bondár I, Engdahl ER, Harris J, Lee WHK, Villaseñor A, Bormann P (2013) Public release of the ISC-GEM Global Instrumental Earthquake Catalogue (1900-2009). Seismol Res Lett 84(5):810–815. https://doi.org/10.1785/0220130034

Tarantola A, Valette B (1982) Inverse problems = quest for information. J Geophys Res 50:159–170

Tirel C, Gueydan F, Tiberi C, Brun J (2004) Aegean crustal thickness inferred from gravity inversion. Geodynamical implications. Earth Planet Sci Lett 228(3-4):267–280. https://doi.org/10.1016/j.epsl.2004.10.023

Tiryakioğlu İ, Aktuğ B, Yiğit CÖ, Yavaşoğlu HH, Sözbilir H, Özkaymak Ç, Poyraz F, Taneli E, Bulut F, Doğru A, Özener H (2018) Slip distribution and source parameters of the 20 July 2017 Bodrum-Kos earthquake (Mw6.6) from GPS observations. Geodin Acta 30(1):1–14. https://doi.org/10.1080/09853111.2017.1408264

Tur H, Yaltırak C, Elitez İ, Sarıkavak KT (2015) Pliocene-Quaternary tectonic evolution of the Gulf of Gökova, southwest Turkey. Tectonophysics 638:158–176. https://doi.org/10.1016/j.tecto.2014.11.008

van der Meijde M, van der Lee S, Giardini D (2003) Crustal structure beneath broad-band seismic stations in the Mediterranean region. Geophys J Int 152:729–739. https://doi.org/10.1046/j.1365-246X.2003.01871.x

VanDecar JC, Crosson RS (1990) Determination of teleseismic relative phase arrival times using multi-channel cross-correlation and least squares. Bull Seismol Soc Am 80(1):150–169

Waldhauser F (2001) HypoDD: a computer program to compute double-difference earthquake locations. USGS Open File Rep., 01-113, 2001

Waldhauser F, Ellsworth WL (2000) A double-difference earthquake location algorithm: Method and application to the northern Hayward fault. Bull Seismol Soc Am 90:1353–1368. https://doi.org/10.1785/0120000006

Wells DL, Coppersmith KJ (1994) New empirical relationships among magnitude, rupture length, rupture width, rupture area, and surface displacement. Bull Seismol Soc Am 8(4):974–100